CHALMERS
UNIVERSITY OF TECHNOLOGY

Wideband mm-wave 6 × 2 Distributed MIMO Transmitter using Sigma-Delta-over-Fiber

Citation for the original published paper (version of record):
Bao, H., Ponzini, F., Fager, C. (2024). Wideband mm-wave 6 × 2 Distributed MIMO Transmitter using Sigma-Delta-over-Fiber. Journal of Lightwave Technology, In Press.
http://dx.doi.org/10.1109/JLT.2024.3356668

Wideband mm-wave 6 × 2 Distributed MIMO Transmitter using Sigma-Delta-over-Fiber

Husileng Bao, *Graduate Student Member, IEEE,* Filippo Ponzini, and Christian Fager, *Senior Member, IEEE*

***Abstract*—This paper investigates a millimeter-wave sigma-delta-over-fiber distributed multiple-input-multiple-output (D-MIMO) solution, in which a central unit connects two remote radio heads (RRH) with two standardized QSFP28 fiber connections. The four subchannels of the QSFP28 carry three individually controlled intermediate frequency (IF) sigma-delta modulated bitstreams and one local oscillation signal to each RRH. At each RRH, the upconversion to mm-wave frequency is performed while maintaining full phase coherence between all channels and distributed RRHs. This solution offers an effective and scalable way to feed multiple radio heads with coherent signals proper for high performance millimeter-wave D-MIMO systems. Wireless performance of the transmitter is experimentally verified by multiple-input-single-output (MISO) and multiple-user MIMO cases in a 1.4 m × 1.6 m area with 748 MHz wideband signals. The comparison with other publications shows that the proposed system is the first millimeter-wave sigma-delta-over-fiber D-MIMO solution that serves multiple users and reaches the largest bandwidth.**

***Index Terms*—Millimeter-wave, MIMO communication, Sigma-delta modulation, radio-over-fiber, central unit, hardware.**

I. Introduction

THE dramatically increasing number of mobile communication devices and rapid growth of data traffic of each device will require wireless network infrastructures supporting tens of Gbps data rate [1] [2]. The mm-wave frequency band offers greater data throughput than the lower bands. Beyond-5G and 6G mobile communication systems will therefore employ millimeter-wave (mm-wave) to a greater extent to meet the capacity demand. However, mm-wave signals suffer from weak penetration and high propagation loss [3], limiting the available communication capacity in practice. Multiple-input-multiple-output (MIMO) concepts can, to some degree, compensate for propagation loss using beamforming and at the same time increase the communication capacity with high spectrum efficiency using spatial diversity [4]. Traditionally, co-located MIMO (C-MIMO) systems are used, with remote radio heads (RRH) physically close to each other. This causes signal interference and limits the overall capacity of C-MIMO [5]. Distributed MIMO (D-MIMO) is an attractive technique to reduce the interference between nearby RRHs by physically distributing them. Theory in [6] and experimental illustrations in [7] show that D-MIMO offers a more uniform capacity to users, and simulations in [8] also illustrate that D-MIMO enhances communication performance in mm-wave frequency bands. The combination of effective interference reduction, uniform coverage, and increased bandwidth makes mm-wave D-MIMO particularly effective in environments requiring a high-capacity network capable of accommodating numerous users with high-bandwidth demands. This is especially applicable in crowded indoor/outdoor events, hyperconnected factories, or stadiums.

Radio-over-Fiber (RoF) architectures are commonly used in current mobile communication systems and also a hot research topic for future communication system implementations [9]. Moreover, in a D-MIMO RoF system, moving the intensive computations into a central unit (CU) and enabling a CU-controlled architecture can drastically simplify the RRH design, as is needed to reduce the overall system deployment cost [10]. The challenge of implementing D-MIMO systems in general, and particularly at mm-wave frequencies, is to maintain coherence between the distributed RRHs while keeping RRH complexity and cost low.

Several mm-wave analog RoF (ARoF) experimental setups [11]–[15] demonstrated optical fiber-connected wireless communication with one remote radio head. The outdoor analog beamforming demonstration in [16] reported a 391 MHz bandwidth transmission at 27 GHz carrier frequency crossing a 160 m over-the-air (OTA) distance. However, the system in [16] included a vector signal generator instrument in the RRH, and does not support coherent transmission between RRHs, as is needed for D-MIMO. The work in [17] studied optical beamforming function by centrally controlling one RRH at 28 GHz center frequency, but only nine fixed beam directions are supported. A simple radio hardware is proposed in [18] where a mm-wave signal is generated in a CU, and used in an ARoF configuration to demonstrate a distributed antenna system with two RRHs operating at 26.5 GHz [19]. However, the system demonstration only had one receiving antenna, corresponding to a single-user multiple-input-single-output (MISO) solution. The highest data rate of 352 Gb/s is recorded using a 141 GHz ARoF system with a 2 × 2 antenna configuration [20]. However, this system is a fixed line-of-sight D-MIMO link, which does not support mobile users. All the transmitter demonstrations reported above rely on complicated and expensive laboratory instruments consisting of Mach-

Manuscript xxxxxxxxxx xxxxxxxxxxxxxxxxxxxxxxxxxxxxx xxxxxxxxxxxxxxxxxxxxxx xxxxxxxxxxxxxxxxxxxxxxx. This project has received funding from the European Union's Horizon 2020 research and innovation programme under the Marie Skłodowska-Curie grant agreement No 860023. *(Corresponding author: Husileng Bao.)*

Husileng Bao and Christian Fager are with the Department of Microtechnology and Nanoscience, Chalmers University of Technology, SE-412 96 Gothenburg, Sweden (e-mail: husileng@chalmers.se; christian.fager@chalmers.se).

Filippo Ponzini is with the GFTL ER HDE Optical Systems, Ericsson Research, IT-561 24 Pisa, Italy (e-mail: filippo.ponzini@ericsson.com).

Color versions of one or more figures in this article are available at https://doi.org/xx.xxxx/JLT.2023.xxxxxxx.

Digital Object Identifier xx.xxxx/JLT.2023.xxxxxx

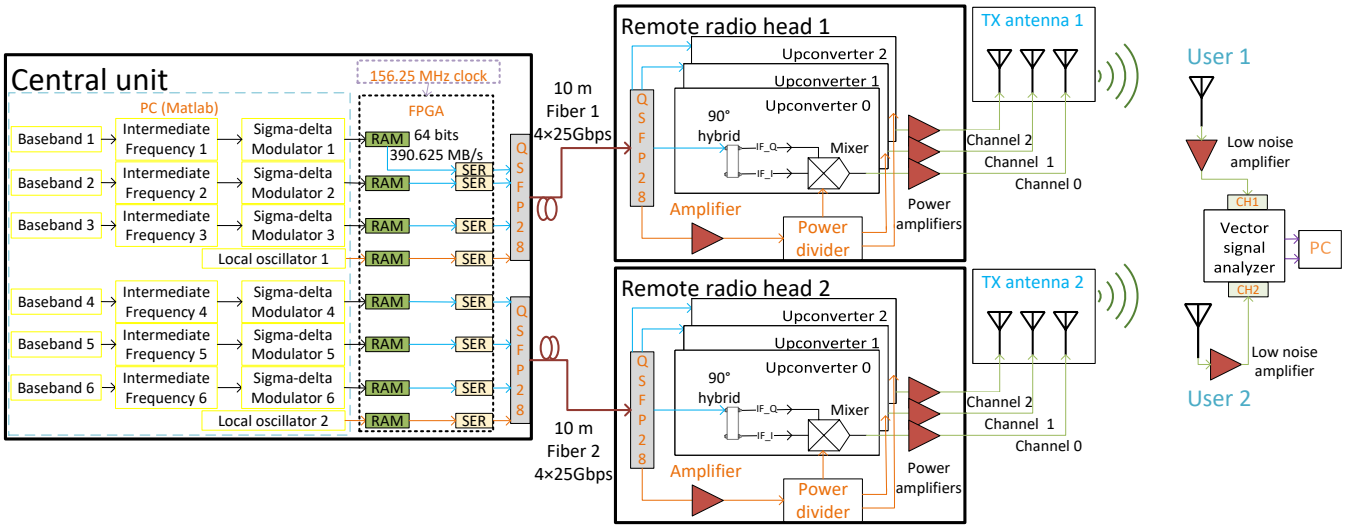

Fig. 1. Proposed millimeter wave transmitter architecture including the receiver used during the experimental characterization. The QSFP28-enabled fibers connect the central unit with the two remote radio heads. At the central unit, the PC and FPGA (VCU128) generate three sigma-delta modulated bitstreams and local oscillator signals to each fiber connection. The remote radio head has three parallel upconversions and power amplifiers to radiate signal through a linear array patch antenna (TX antenna: transmitting antenna). There are two independent users for the following MISO and MIMO demonstrations.

Zehnder modulators, high-speed arbitrary waveform generators, and external lasers. For real D-MIMO deployments, a low-cost and scalable mm-wave RoF solution is needed. A mature ARoF mm-wave MIMO system with 1 GHz bandwidth at 28 GHz carrier frequency is reported in [21]. However, the ARoF solutions suffer from optical signal distortion and dynamic range problems inherent to ARoF systems [22]. The 8 × 4 D-MIMO system in [23] reported the highest spectrum efficiency with 100 MHz bandwidth at 28 GHz. However, it relies on complex RRHs including both analog and digital signal processing blocks.

An alternative to use mm-wave ARoF is to employ sigma-delta-over-fiber (SDoF) architectures, as suggested by the comparison from [24]. A SDoF study implemented 5 Gsps real-time sigma-delta-modulation (SDM) on FPGA and reached 252 MHz bandwidth at fiber connected back-to-back measurement [25]. Another experimental SDoF employed 4-level high-pass SDM at 44 Gsps ,and reported 2.4 GHz bandwidth with 25 GHz carrier frequency in back-to-back demonstration [26]. The experimental works in [27]–[29], demonstrated at 300/370/320 GHz, show that the SDoF solution is scalable to sub-terahertz frequencies. The SDoF system in [30] worked within a 22.75 – 27.5 GHz carrier frequency range. However, it only supported 390 MHz bandwidth from an excessive 100 Gbps bitrate. Another SDoF-based mm-wave 2 × 1 MISO system was proposed in [31] with 160.32 MHz bandwidth across 24 - 29 GHz frequency range. However, the demonstration performance is limited by the 10 Gbps data rate of the fiber connection and phase noise of the phase-locked loop (PLL) used [31]. In addition, the RRH structure is complicated as it requires a clock data recovery (CDR), clock divider, and a PLL [31]. In other words, a wideband mm-wave D-MIMO RoF transmitter for multiple mobile users is still not available.

In [32] and [33], the authors introduced a flexible bandpass- and a wideband lowpass SDoF-based mm-wave transmitter architectures, respectively, based on commercially available off-the-shelf hardware components. A 500 MHz bandwidth co-located multi-user MIMO (MU-MIMO) link was presented in [34], which could serve as a building block in the realization of mm-wave D-MIMO systems.

In this paper, a novel low-cost and low-complexity mm-wave SDoF D-MIMO transmitter architecture is proposed. The architecture utilizes a CU-inherited LO generation and low-noise distribution to guarantee coherence to multiple mm-wave RRHs. A comprehensive study of the hardware impairments and intrinsic performance limitations is reported utilizing an OFDM 64-QAM signal with up to 748 MHz bandwidth. The experiments successfully demonstrate wideband multiple-input-single-output (MISO) for a 1.4 m × 1.6 m area, and MU-MIMO OTA communication. Overall, the results prove the feasibility of the proposed architecture for the implementation of wideband multi-user D-MIMO communication, and thus as a candidate for the realization of next-generation high-capacity wireless networks.

This paper is structured as follows: Section II first explains the transmitter principle. Thereafter, Section III is focused on comprehensive transmitter verification by measurements. Section IV presents OTA communication experiments with MISO and MIMO cases. Finally, conclusions are drawn in Section V.

II. Transmitter Principle

This section starts with introducing the hardware structure for the proposed transmitter architecture. Later, the channel estimation and precoding steps will be presented.

A. Transmitter Architecture

Fig. 1 illustrates the general transmitter architecture proposed, exemplified with the case of two RRHs connected to a CU. The CU includes a PC (MATLAB) and a field

programmable gate array (FPGA) board. In the PC, OFDM 64-QAM modulated baseband signals are generated. Then, the baseband signal is numerically upconverted to an intermediate frequency (IF). The following second-order bandpass SDM (BPSDM) generates bitstreams at 25 Gbps data rate from the IF signal. The signal processing mentioned above is done in MATLAB using the SDM toolbox [35].

The FPGA board (Xilinx Virtex UltraScale+ HBM VCU128) is responsible for transmitting the IF SDM bitstreams through off-the-shelf high-speed QSFP28-fiber optical interconnect links. There are eight random access memory (RAM) blocks for the offline bitstreams and eight serializers (SER) for converting low-speed bytes (64 bits at 390.625 MB/s) to high-speed streams (25 Gbps). The FPGA resource utilization is reported in Table. I. At the FPGA board, all signals are referenced to one shared onboard oscillator (156.25 MHz clock), thereby facilitating coherency between the distributed fiber links. Each QSFP28 fiber link provides four parallel high-speed digital channels with 25 Gbps each. Three of the channels are used to transmit IF SDM bitstreams, and one channel transmits periodic zeros and ones acting as LO signals for the RRH upconverters. In this way, the proposed D-MIMO transmitter architecture results in CU-synchronized RRHs.

TABLE I
FPGA RESOURCE UTILIZATION.

Resource	Utilization	Available	Utilization (%)
lookup table	15506	1303680	1.19
LUTRAM[a]	4946	600960	0.82
Flip-flop	14526	2607360	0.56
BRAM[b]	440	2016	2186
Input/output	16	624	2.56
Gigabit SerDes[c]	8	96	8.33
Global buffer	6	1008	0.60
MMCM[d]	1	12	8.33

[a] lookup table random access memory.
[b] Block random access memory.
[c] Serializer/deserializer.
[d] Mixed-mode clock manager.

Each of the fiber connections is a 10m (Multifiber Termination Push-on/Pull-off) MTP-12 (female) to MTP-12 (female) cable with twelve OM4 multimode fibers, four of which are used in the transmitter. As shown in Fig. 1, each of the RRHs contains three parallel upconversion mixers (Analog Devices ADMV-1013) fed with the three incoming BPSDM coded IF signals, three 90° hybrids, and three mm-wave power amplifiers (PAs, Analog Devices EVAL-HMC943APM5E). The 90° hybrids are used to feed the mixers with a quadrature IF signal for single sideband upconversion. Generally, a bandpass filter is required at the RRH to recover the analog IF signal from the BPSDM signal. However, in our application, the 90° hybrid and the IF input of the mixer has a bandpass filter (0.8 GHz - 6 GHz), suppressing the majority of the out-of-band quantization noise. For the generated SDM bitstreams (25 Gbps), the dominating quantization noises are located for frequencies higher than 6 GHz. We mainly wanted to push the maximum achievable bandwidth which is the desire for high-frequency communications. If we want a fixed narrow bandwidth for a specific application, it is recommended to have an IF filter. Additionally, each RRH contains LO amplifiers and power dividers to guarantee coherence between the RRH channels and sufficient power level to drive the upconversion mixers. In our system, the LO is generated by sending periodic zeros and ones in the LO channel (11001100...). The lane rate of 25 Gbps results in a fixed LO frequency of 6.25 GHz and harmonic frequency at 12.5 GHz. The LO amplifiers (Analog Devices EVAL-HMC3587LP3B) operate at 4 GHz - 10 GHz with 18.1 dB gain. The upconversion mixers include quadruplers, and accept LO frequencies with a bandpass filter in the range 5.4 GHz - 10.25 GHz. In this implementation, a 1.5 GHz IF signal, which combined with the 6.25 GHz LO frequency, results in an upper sideband output frequency of 26.5 GHz according to 6.25 GHz $\times$ 4 + 1.5 GHz = 26.5 GHz.

The TX linear patch antenna array is designed in CST Microwave Studio for 28 GHz center frequency but works at 26.5 GHz in this study. Fig. 2 shows the TX antenna geometry with radiation patterns. Each column of the antenna has four fixed patch elements, which create a 80.6°/41.5° 3 dB beam width in the azimuth/elevation direction at 26.5 GHz, respectively. Each TX antenna has four independent feeding ports, with three of them fed with the three parallel coherent signals from the RRH as labeled in Fig. 2. Therefore, the antenna enables the CU-controlled digital beam steering function in azimuth direction.

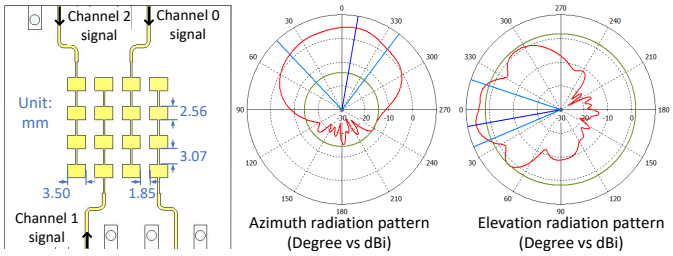

Fig. 2. Antenna schematic and radiation patterns (at 26.5 GHz) for one of the columns (channel 2) for the proposed transmitter. The blue lines in the radiation patterns represent the main beam and 3 dB beamwidth directions, respectively.

B. OFDM MIMO Processing

The proposed D-MIMO architecture will be utilized to demonstrate both MISO and MU-MIMO experiments. The necessary signal processing steps are reviewed here. In our measurements, channel estimation is the first step, followed by MIMO communication, as presented in Fig. 3. To demonstrate wideband transmission with nonflat frequency responses, we will use OFDM 64-QAM modulation scheme with the parameters reported in Table II. The MIMO transmitter signal processing steps include filtering, upsampling, and upconversion of the OFDM signal before applying SDM. The shaping/matching filter at the transmitter/receiver side is a root-raised cosine filter with a 0.2 roll-off factor. The MIMO receiver performs offline frequency/timing synchronization before the final OFDM demodulation step.

The CU generates OFDM pilot signals to the RRH at the channel estimation step. Following the same OFDM pilot principle as in [31], this transmitter needs to transmit 6 OFDM

TABLE II
OFDM SIGNAL PARAMETERS.

Parameter	Value
FFT size	1024 subcarriers
DC	null
Guard band 1	121 subcarriers
Guard band 2	122 subcarriers
Cyclic prefix	128 samples
Subcarrier number	780 subcarriers
Bandwidth (MHz)	93.6 187.2 280.8 374.4 468 561.6 655.2 748.8
Subcarrier spacing (KHz)	120 240 360 480 600 720 840 960

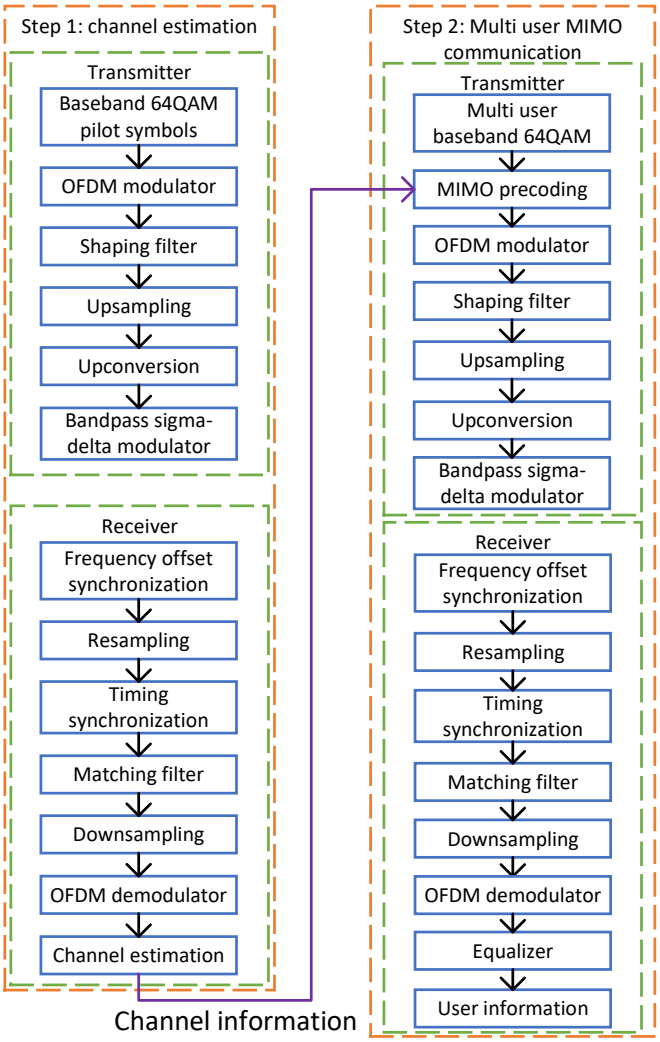

Fig. 3. Signal processing steps of OFDM 64-QAM signal for the over-the-air MU-MIMO measurements.

symbols, where non-zero subcarriers are quadrature phase shift keying (QPSK) pilot signal. To capture the pilot transmission at one time and estimate the channel for each transmitting antenna separately, the resulting OFDM pilot symbol becomes

$$\mathbf{X} = \begin{bmatrix} x_1 & 0 & .. & 0 & 0 & .... & 0 \\ 0 & x_2 & .. & 0 & x_{K+1} & .... & 0 \\ 0 & 0 & .. & 0 & 0 & .... & 0 \\ .. & .. & .. & .. & .. & .... & .. \\ .. & .. & .. & .. & .. & .... & x_{K\times N} \\ 0 & 0 & .. & x_K & 0 & .... & 0 \end{bmatrix} \tag{1}$$

$\mathbf{X}$ has a dimension of $N \times (N \times K)$, where N is the channel number of TX antennas, which equals the number of OFDM symbols, and K is the number of subcarriers.

For each subcarrier i, M users receive a signal of $\mathbf{Y}_i$. Hence, the channel model is

$$\begin{bmatrix} y_1 \\ y_2 \\ .. \\ y_M \end{bmatrix}_i = \begin{bmatrix} h_{11} & .. & h_{1N} \\ h_{21} & .. & h_{2N} \\ .. & .. & .. \\ h_{M1} & .. & h_{MN} \end{bmatrix}_i \begin{bmatrix} x_{K\times 0+i} \\ x_{K\times 1+i} \\ x_{K\times 2+i} \\ .. \\ x_{K\times (N-1)+i} \end{bmatrix}_i + \begin{bmatrix} w_1 \\ w_2 \\ .. \\ w_M \end{bmatrix}_i \tag{2}$$

$$\mathbf{y}_i = \mathbf{H}_i \mathbf{x}_i + \mathbf{w}_i, \tag{3}$$

where $i = 1 \cdots K$, $\mathbf{H}_i$ is the channel matrix for the ith subcarrier channel and $\mathbf{w}_i$ is additive noise. $\mathbf{y}_i$ and $\mathbf{w}_i$ have a dimension of $M \times 1$, $\mathbf{H}_i$ have a dimension of $M \times N$, representing the number of RX and TX antennas, respectively. $\mathbf{x}_i$ is a $N \times 1$ vector corresponding to the channel number of TX antennas.

The channel matrix estimation for subcarrier i, $\widehat{\mathbf{H}}_i$, is obtained from a least-square estimation

$$\widehat{\mathbf{H}}_i = \left(\mathbf{x}_i^{\mathrm{T}} \mathbf{x}_i\right)^{-1} \mathbf{x}_i^{\mathrm{T}} \mathbf{y}_i. \tag{4}$$

In the experiments, a zero-forcing (ZF) precoder has been used. The ZF precoder for subcarrier i, $\mathbf{P}_i$, is defined as

$$\mathbf{P}_i = \left(\widehat{\mathbf{H}}_i \widehat{\mathbf{H}}_i^*\right)^{-1} \widehat{\mathbf{H}}_i. \tag{5}$$

The ZF algorithm processes the user data at subcarrier i, $\mathbf{u}_i$, to generate the MIMO signals, $\mathbf{s}_i$, according to

$$\mathbf{s}_i = \mathbf{P}_i \mathbf{u}_i. \tag{6}$$

In this demonstration, $\{M, K, N\}$ is $\{2{,}780{,}6\}$ for the MIMO procedure. For the MISO case, the channel estimation and precoding procedures are still the same as in the MIMO case, with $M = 1$.

III. TRANSMITTER VERIFICATION

The proposed D-MIMO transmitter architecture shown in Fig. 1 has been implemented as shown in Fig. 4. Two TX antenna arrays (see Fig. 2), each connected to a RRH, are mounted on identical structures and physically separated by a distance of 55 cm. The receiving antennas are home-made Vivaldi antenna and designed in CST Microwave Studio. Two low-noise amplifiers connect the receiving antennas with two separate channels of an oscilloscope (Keysight UXR0334A Infiniium UXR-Series: 33 GHz, 4 Channels equipped with a vector signal analyzer software Keysight VSA 89600). The experimental investigations presented in this section cover the LO signal phase noise, power levels at each stage in the transmitter chain, system coherence, and bandwidth performance.

In Table III, a list of the hardware used for the transmitter is presented. All of them are commercially available.

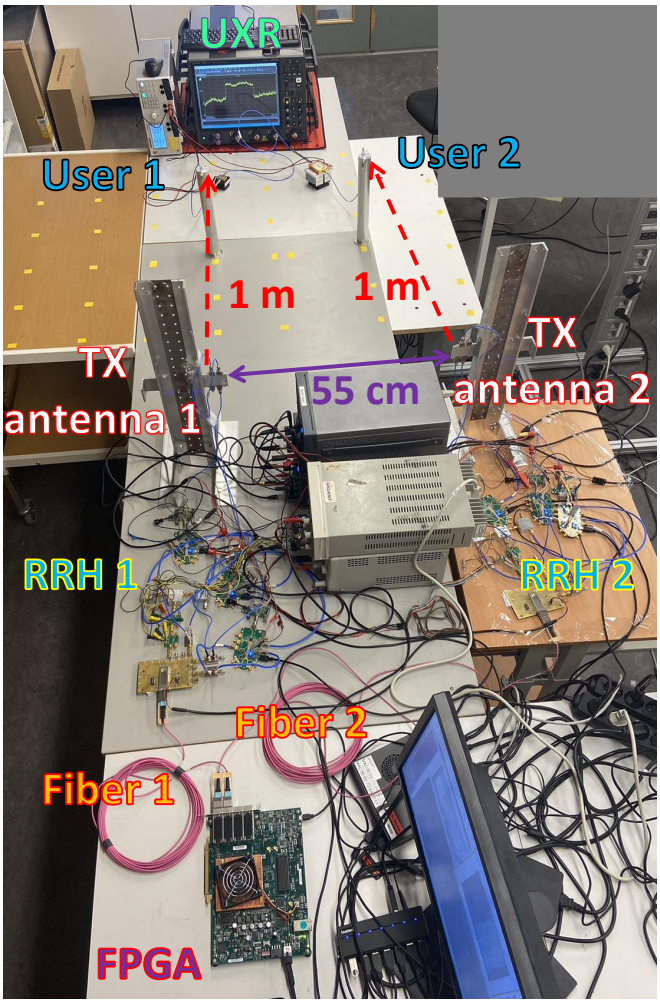

Fig. 4. Measurement setup for investigation of the proposed transmitter. The two transmitting antennas are separated by 55 cm. The yellow labels attached to the bench indicate the user positions where over-the-air measurements were carried out.

TABLE III
LIST OF COMMERCIAL TRANSMITTER HARDWARE.

Hardware	Manufacturer	Model	Quantity
FPGA board	Xilinx	VCU128	1
QSFP28	FS	QSFP28-SR4-100G	4
90° Hybrid	Mini-Circuits	ZX10Q-2-19-S+	6
Power divider	Mini-Circuits	ZX10R-14-S+	6
Mixer	Analog Devices	EVAL-ADMV1013	6
LO amplifier	Analog Devices	EVAL-HMC3587LP3B	4
Power amplifier	Analog Devices	EVAL-HMC943APM5E	6

TABLE IV
TECHNICAL SPECIFICATIONS OF QSFP28 MODULE.

Specification	Description	Specification	Description
Wavelength	850 nm	Connector	MTP[a]-12
Media	Multi-mode fiber	Max fiber length	100 m
TX Type	VCSEL[b]	Receiver Type	PIN[c]
TX Power	-8.4 to 2.4 dBm	Max Data Rate	4x25.78 Gbps

[a] Multifiber Termination Push-on/Pull-off.
[b] Vertical Cavity Surface Emitting Laser.
[c] Positive-Intrinsic-Negative photodiodes.

Table IV summarizes the key technical specifications of the QSFP28 module used for the fiber connection. The selected QSFP28 module supports a maximum fiber length of 100 m although, in our implementation, the length is limited to 10 m.

A. Local Oscillator Signal Quality

As mentioned in Section II. A, in this work, the CU generates two identical periodic bitstreams consisting of repeated two ones and two zeros, which are transported to the two RRHs using a dedicated channel.

The binary LO signal arriving at the RRH has strong harmonic content. However, this is not a problem in this implementation because of the passband filter response of the LO amplifier, power dividers, and the LO input of the mixer. The inband power was obtained from the vector signal analyzer (VSA) measurements. The power of the fundamental component of the LO signal generated from the QSFP28 module is -7.7 dBm, as shown in Fig. 5, while the mixer requires an LO input with a power in the range of -6 to 6 dBm. An LO amplifier is therefore inserted to deliver 0.4 dBm LO signal power to the mixer, after approximately 10 dB of loss from the power dividers and the coaxial cable connections.

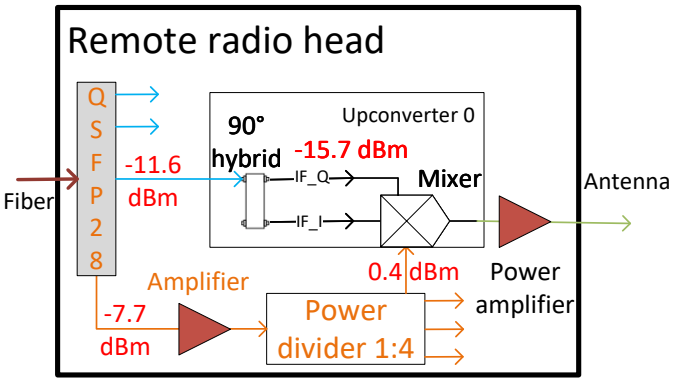

Fig. 5. Measured inband power levels of the local oscillator and OFDM signals in the RRH.

The LO- and reference signals are sampled by the oscilloscope at 128 Gsps, resulting in the phase noise spectrum in

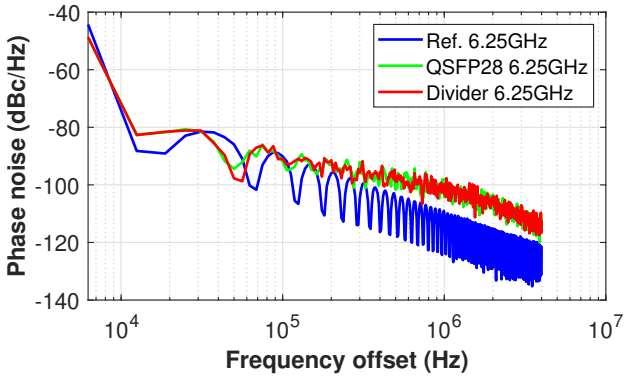

Fig. 6. Phase noise characterization of the proposed local oscillator signal at QSFP28/power divider output, and a reference signal synthesizer.

Fig. 6. The phase noise of this LO signal is compared with a reference signal from a signal synthesizer (Agilent E8267D). At a 1 MHz offset, the phase noise of the CU-generated and QSFP28-distributed LO is approximately 5 dB worse than that of the signal generator. Furthermore, two generated LO signal curves from the QSFP28 and the power divider output overlap, which means that the LO amplifier does not contribute with additional phase noise.

B. OFDM Signal Power Levels

We investigated the average inband power levels with an OFDM 64-QAM signal at different positions in the RRH. The measured inband power of the IF signal at the output of the QSFP28 receiver is -11.6 dBm, and it is the same for all the QSFP28 output signals. With the power loss of 90° hybrid, SMA connector and coaxial cable, the IF input of the mixer is reduced to -15.7 dBm inband power. The upconversion mixer chip used can provide up to 18 dB gain to the price of nonlinear distortion if high gain settings are used. The EVM performance with different output power levels is reported in Fig. 7. It is important to note that the instantaneous peak power is 8.3 dB higher than the inband mixer output power reported above due to the peak-to-average power ratio (PAPR) of the OFDM 64-QAM signal.

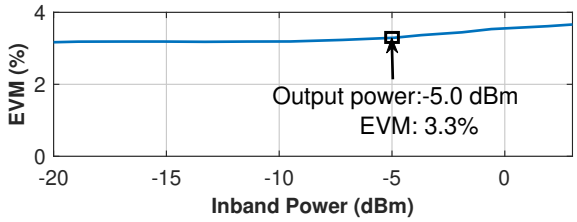

Fig. 7. Output signal performance of the active mixer as the output inband power is increased by changing the gain setting.

By observing the results in Fig. 7, we decided to operate the mixer at an average output power of -5.0 dBm, as a good compromise between output power and nonlinearity. From Fig. 8(a), it is shown that the adjacent channel power ratio (ACPR) at the output of the mixer is -35.7 dBc. Fig. 8(b) shows that the output power and ACPR of the mm-wave power amplifier are 17.3 dBm and -35.7 dBc, respectively. From this, we can conclude that the ACPR is barely changed before and after the power amplifier, meaning that it works in its linear regime. Furthermore, the power difference of 22.3 dB = 17.3 dBm - (-5.0 dBm) proves that the gain of the power amplifier matches the datasheet specification. The spectra in Fig. 8 have a sinusoidal peak at the right side of the signal band, which is used for carrier frequency offset synchronization in the RX signal processing.

The output spectrum at the output of one channel of the RRH is reported in Fig. 9. The inband signal is 25 dB higher than the lower sideband, the quantization noise, and the LO signal leakage. The suppression could be further improved by installation of dedicated IF bandpass filters after the QSFP28 and/or mixer stages in the RRH. It shows that the output signal does not have any spurious problems.

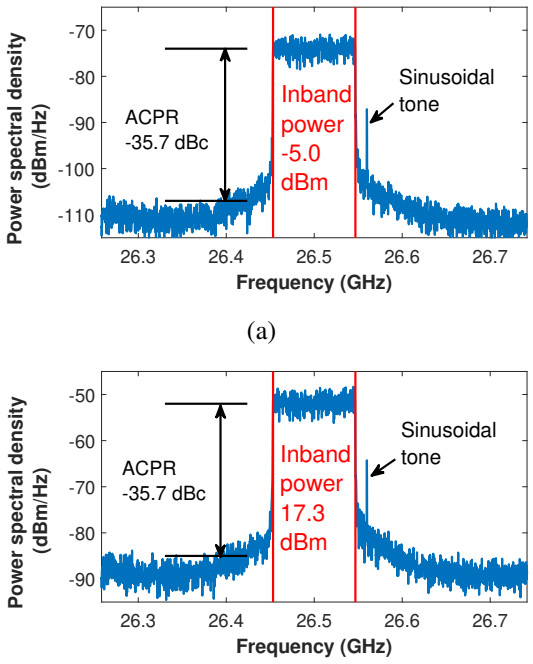

Fig. 8. Signal spectrums with inband power and lower adjacent channel power ratio (ACPR). The sinusoidal tone at the right side is used for frequency offset synchronization in the receiver signal processing. (a) Output signal spectrum of the mixer. (b) Output signal spectrum of the power amplifier.

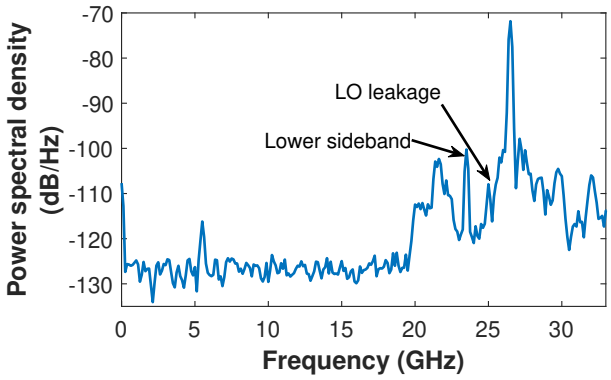

Fig. 9. Wideband spectrum at the output for one channel of the RRH.

C. Bandwidth Performance

This section investigates the bandwidth performance of the transmitter. During the investigations, an ideal BPSDM simulation is included as a reference in Fig. 10. The results are ultimately limited by the quantization distortion induced by the oversampling ratio and the second-order BPSDM modulation used. For a fixed BPSDM sample rate of 25 Gsps, the EVM is degrading as the bandwidth increases from 93 MHz to 748 MHz, corresponding to the oversampling ratio decreasing from 268.8 to 33.4. As Fig. 10 shows, for the 1.5 GHz IF signal used, the QSFP28 output and IF input of the mixer have the same EVM performance, only with an inband power difference. The performance difference between the IF signal measurements and the simulations is explained by

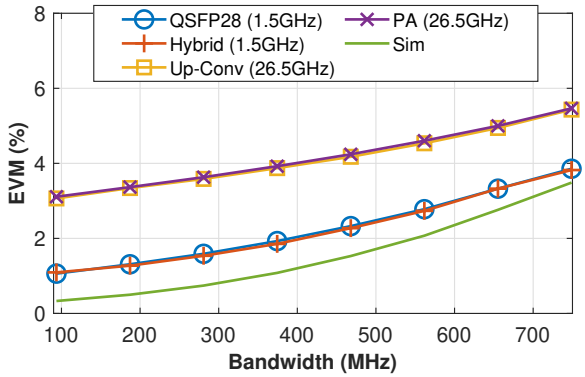

Fig. 10. Bandwidth performance in each stage of one channel of the RRH. The error vector magnitude (EVM) for an ideal sigma-delta modulated simulation is included as a reference (Sim).

the hardware limitations of the FPGA and fiber link. On the other hand, after mixer upconversion, the mm-wave signals (26.5 GHz) have worse EVM performance than the IF signals due to the addition of LO phase noise, as studied in Section III. A. It is important to note that the PA does not introduce any significant distortion since the mixer and PA output curves overlap. In summary, the transmitter is able to support a 748 MHz wideband OFDM 64-QAM signal with a 5.5% EVM performance.

D. Remote Radio Head Coherence

System coherence is crucial in D-MIMO RoF systems [36] [37]. This section studies the system coherence at phase level with the setup shown in Fig. 11. From the common 25 Gbps bitrate, the CU generates 6.25 GHz LO signals, as described previously. Moreover, there are 1.5625 GHz sinusoidal IF signals from the CU with the same method by repeating eight ones and eight zeros.

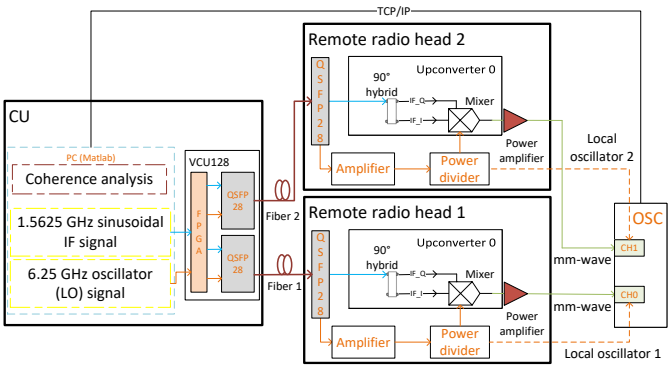

Fig. 11. LO and millimeter wave signal measurement setup for coherence analysis.

In the first experiment, the oscilloscope (Keysight UXR0334A) samples simultaneously LO signals extracted from two RRHs at 128 GSa/s. For the coherence analysis, the amplitude and phase of the LO signals are extracted by numerical down conversion of the oscilloscope samples, as reported in Fig. 12(a)(c). Secondly, the oscilloscope simultaneously samples the mm-wave (26.5625 GHz) sinusoidal signals, from RRH1:channel 0 and RRH2:channel 0, at 128 GSa/s. The coherence analysis results are reported in Fig. 12(b)(d). In Fig. 12(a)(b), we normalized the phase and amplitude of channel 1 to channel 0, using a dataset of 11,000,000 oscilloscope samples. The polar plots show that the amplitude is always similar between two channels for both the LO and mm-wave signals, while the mm-wave polar plot (Fig. 12(b)) has greater phase variation than the LO polar plot Fig. 12(a). The normalized relative phase variation probabilities in Fig. 12(c)(d) have standard deviations of 1.52° and 6.28° for the LO signals and the mm-wave signals, respectively. This mm-wave standard deviation of 6.28° can match with a theoretical prediction based on incoherent addition of the noise in the IF and four times multiplied LO signals (4 × LO + IF = mm-wave) by setting the respective values in

$$\sigma_{\mathrm{mm-wave}} = \sqrt{{\sigma_{\mathrm{IF}}}^2 + (\sigma_{\mathrm{LO}} \times 4)^2}, \tag{7}$$

where $\sigma_{LO} = \sigma_{IF} = 1.52°$. This results in $\sigma_{mm-wave} = 6.27°$, which is in close agreement with the results from the measurement. In summary, the measurements in this section have verified that the proposed transmitter architecture can support a wideband, linear, and coherent transmission of communication signals for D-MIMO systems.

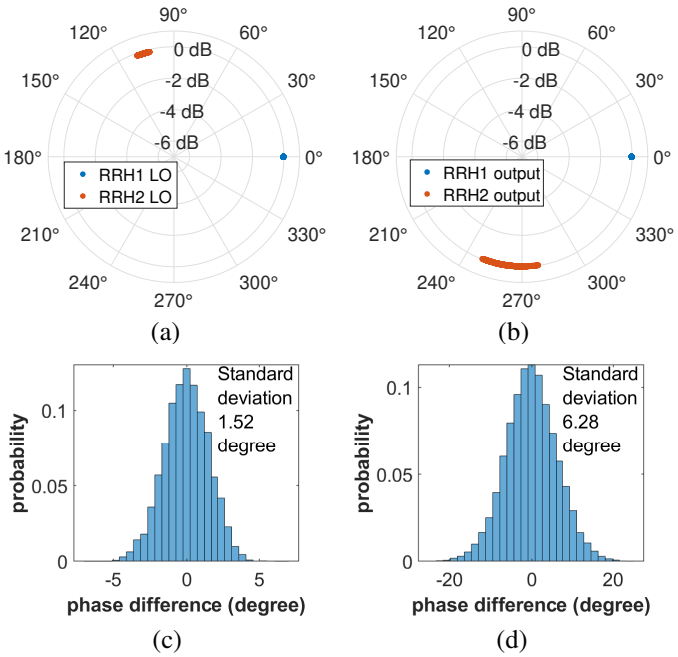

Fig. 12. System coherence. (a) Polar plot of the local oscillation signal. (b) Polar plot of the millimeter wave signals (from RRH1:channel 0 and RRH2:channel 0). (c) Normalized phase coherence of the local oscillation signal. (d) Normalized phase coherence of the millimeter wave signal (from RRH1:channel 0 and RRH2:channel 0).

IV. OTA Communication Experiments

In the following section, we will report OTA experiments demonstrating how the transmitter architecture presented in previous sections can be used for single- and multiple-user experiments.

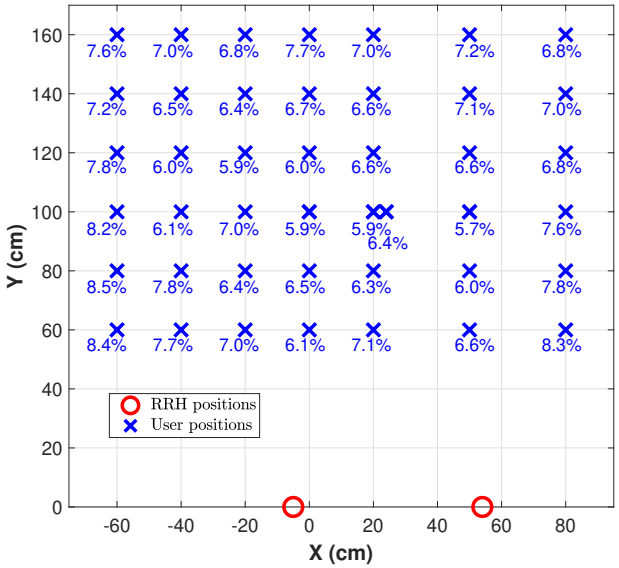

Fig. 13. Error vector magnitude (EVM) coverage of the MISO measurements with 748 MHz bandwidth signal at 43 labeled positions as shown in Fig. 4.

A. Single User MISO Coverage

The MISO measurement are performed in a 1.4 m × 1.6 m area at the marked positions shown in Fig. 4. The independent receiving antennas are freely moveable in the area for measurement. At each position, channel estimation and precoding are carried out with a 748 MHz bandwidth OFDM signal, as introduced in Section II.C. In the first step, the pilot signals defined in (1) are transmitted for channel estimation according to (4). In the second step, the transmitter transmits ZF-precoded data using the expressions in (5) and (6).

Fig. 13 shows the RRH and user locations used for this and subsequent experiments. The numbers reported in Fig. 13 correspond to the EVM in the MISO experiments. Most of the positions satisfy the 8% EVM requirement for OFDM 64-QAM signal set in the 3GPP [38]. A few of the peripheral positions have worse EVM, occurring when the users are located at the limits of the antenna coverage area. Around the center area, the EVM is better than 6%. This is the area where the following MU-MIMO experiments are performed. This OTA demonstration area is related to the signal bandwidth, the output power, and the antenna gain. With the current setup, narrow bandwidth can support larger area without performance degradation. For 748 MHz bandwidth signal, either the RRH output power or the antenna gain need to be improved to reach a larger area.

B. Two User MU-MIMO Performance

In the MU-MIMO measurements, two RRHs, each with three individually fed channels, serve two independent users simultaneously. In Case 1, the two users are separated by a distance of 50 cm, while they are separated by merely 5 cm in Case 2 (see Fig. 14). For each case, as explained in Section II.B, the transmitter first radiates pilot signals for least-square channel estimation and then starts transmission of

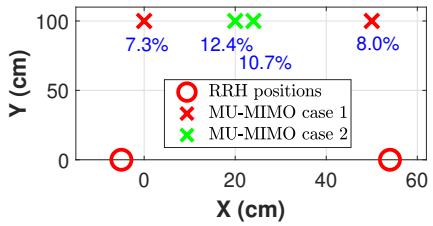

Fig. 14. User and RRH positions for MU-MIMO measurements with error vector magnitude (EVM) for 748 MHz bandwidth signal.

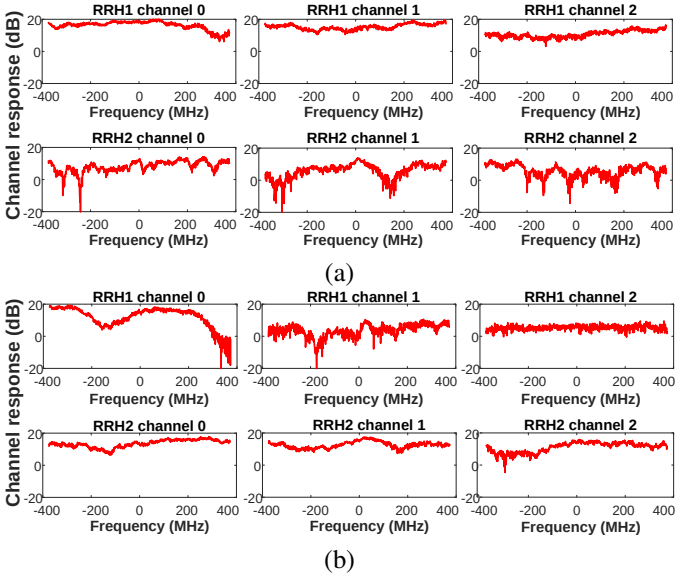

Fig. 15. Channel response between the two RRHs and one of the users in MU-MIMO Case 1: (a) User 1. (b) User 2.

ZF-precoded user data. The 748 MHz bandwidth MU-MIMO measurements have worse EVM results than the previous MISO measurements at the corresponding locations since the ZF-precoder allocates lower power per user in the two-user cases.

Fig. 15 shows the magnitude of the channel response for Case 1 at 748 MHz bandwidth with 780 subcarriers. Fig. 15 shows that the channels have significant frequency variations, thus illustrating the need for frequency domain channel estimation and precoding using OFDM in wideband applications.

In both MIMO measurement cases, the bandwidth is swept from 93 to 748 MHz with the EVM results reported in Fig. 16. In general, both cases work for two users. Specifically, Case 1 serves the two users with better EVM than in Case 2, due to the

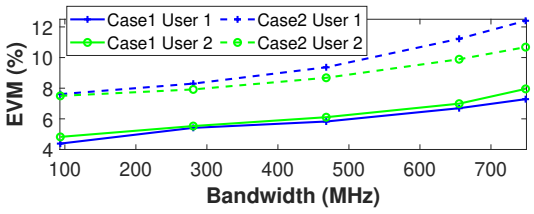

Fig. 16. Error vector magnitude (EVM) results from the MU-MIMO measurements with different bandwidths.

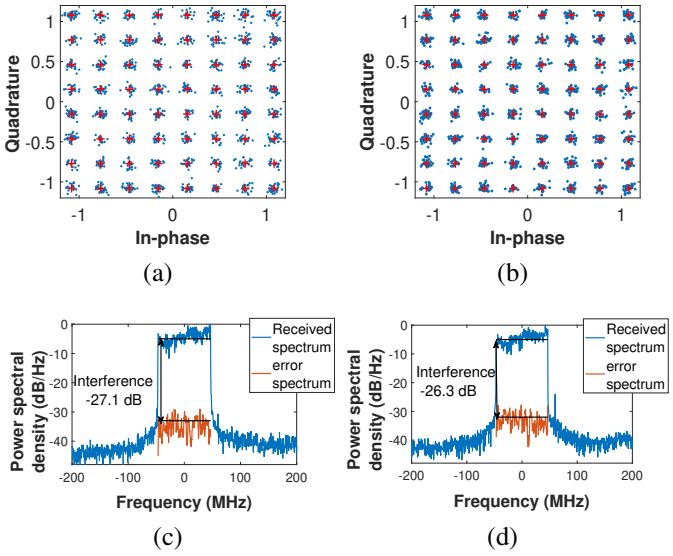

Fig. 17. Constellation and interference of MU-MIMO Case 1 at 93 MHz bandwidth. (a) Constellation of User 1; (b) Constellation of User 2. (c) Interference of User 1; (d) Interference of User 2.

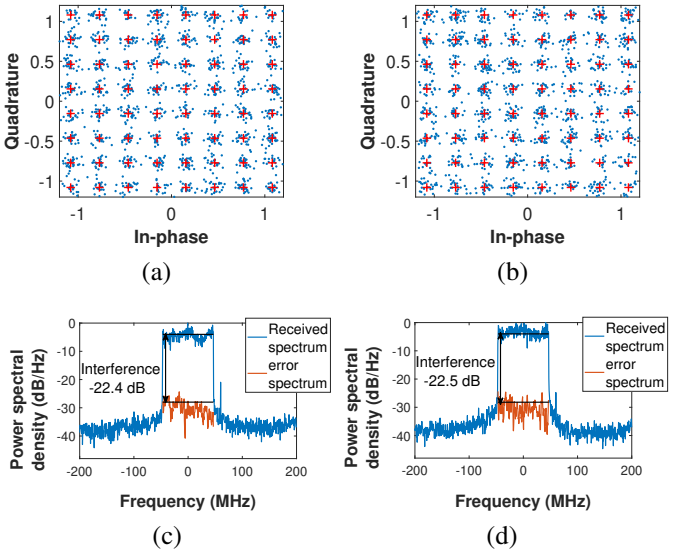

Fig. 19. Constellation and interference of MU-MIMO Case 2 at 93 MHz bandwidth. (a) Constellation of User 1; (b) Constellation of User 2. (c) Interference of User 1; (d) Interference of User 2.

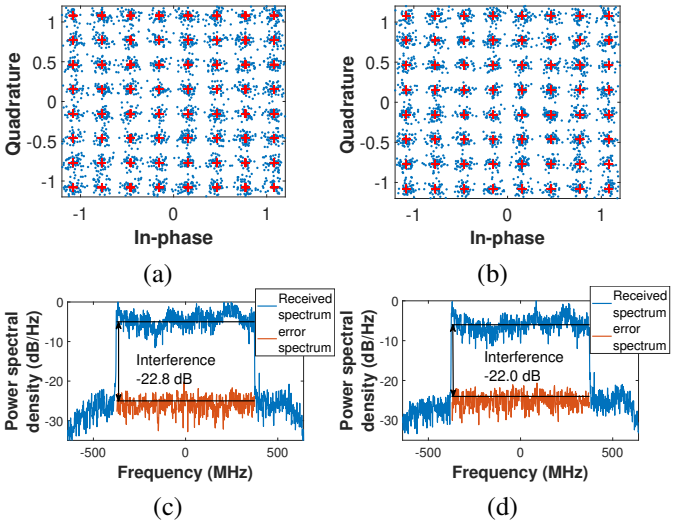

Fig. 18. Constellation and interference of MU-MIMO Case 1 at 748 MHz bandwidth. (a) Constellation of User 1; (b) Constellation of User 2. (c) Interference of User 1; (d) Interference of User 2.

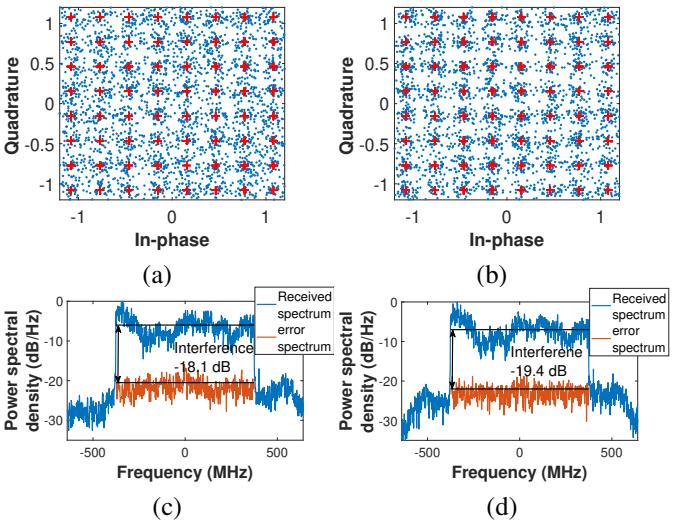

Fig. 20. Constellation and interference of MU-MIMO Case 1 at 748 MHz bandwidth. (a) Constellation of User 1; (b) Constellation of User 2. (c) Interference of User 1; (d) Interference of User 2.

channel diversity of more separated user positions. Moreover, in Case 1, both users can satisfy the EVM requirements of the 3GPP specifications [38] for OFDM 64-QAM signal up to 748 MHz bandwidth and have similar performance for the two users as promised by the ZF precoding scheme used. Fig. 17(a)(b) presents the constellation diagrams from the 7020 symbols transmitted, which is sufficient for the accurate EVM calculations.

We have studied inter-user interference of the MU-MIMO measurements by comparing the error spectrum with the received spectrum, as explained in [34]. The error spectrum is a frequency domain representation of the difference between the demodulated constellation and the reference constellation for users. The corresponding spectra in Fig. 17(c)(d) presents inter-user interference for MU-MIMO Case 1 with 93 MHz bandwidth, which shows that the inband error spectrum is higher than the out-of-band noise level of the received signal and has a distinct frequency response. This can not be explained by nonlinear distortion since there is no sign of out-of-band distortion sidebands. This means that the inband distortion is caused by inter-user interference in the MU-MIMO transmission Case 1. At a 93 MHz bandwidth, the two users have an inter-user interference level of -27.1 dB/-26.3 dB, respectively, which dominates the overall MU-MIMO transmission performance. Fig. 19 presents the same analysis for the MU-MIMO Case 2, where the inter-user interference is

TABLE V
COMPARISON WITH THE STATE-OF-THE-ART MIMO ROF PUBLICATIONS.

Ref.	RoF	MIMO	Bandwdith	Modulation	OTA distance	Carrier frequency	NMSE
[39]	ARoF	2 × 2	1 GHz	64-QAM OFDM	10 m	28 GHz	-24.3 dB
[17]	ARoF	9 × 1	100 MHz	64-QAM OFDM	6.3 m	28 GHz	-31.3 dB
[20]	ARoF	2 × 2[a]	22 GHz	16-QAM	0.2 m	140 GHz	-14 dB
[40]	ARoF	2 × 1	3 GHz	64-QAM	1.5 m	28 GHz	-23 dB
[41]	ARoF	8 × 1	3.5 GHz	16-QAM	0.5 m	60 GHz	-19.6 dB
[41]	ARoF	8 × 4	100 MHz	QPSK OFDM	8.5 m	28 GHz	-22 dB
[31]	SDoF	2 × 1	160.32 MHz	64-QAM OFDM	2.0 m	> 24 GHz	-24.4 dB
This work	SDoF	6 × 1	748 MHz	64-QAM OFDM	1.6 m	26.5 GHz	-25.2 dB
This work	SDoF	6 × 2	748 MHz	64-QAM OFDM	1.0 m	26.5 GHz	-22 dB

[a] This is only antenna configuration and does not have MIMO precoding.

increased to -22.3 dB/-23.3 dB inter-user interference for MU-MIMO transmission. The increased inter-user interference in Case 2 is caused by ill-conditioning of the channel matrix as the user positions are closer. Fig. 18 and Fig. 20 are the same analysis for 748 MHz bandwidth measurements. The spectra in Fig. 18(c)(d) and Fig. 20(c)(d) are from a sample rate of 1.28 Gsps and 1 GHz bandwidth of the equipped VSA software configuration. Therefore, The spectra can not do the out-of-band analysis but do not show inband non-linear distortions. Furthermore, the two users have inter-user interference levels of -22.8 dB/-22.0 dB and -18.1 dB/-19.4 dB for 748 MHz at Case 1 and Case 2, respectively.

C. Comparison with the State-of-The-Art

The results obtained in this work are compared to state-of-the-art demonstrations in Table V. Most of the publications reported were ARoF MIMO demonstrations, while [31] is the only one SDoF MISO reference, although with a limited bandwidth. For multi-user demonstrations, all of them work with OFDM signal, which is also the case in this work. Moreover, this work is the only one using low-complex SDoF technology and reports 748 MHz bandwidth for spectrum-sharing MU-MIMO SDoF demonstrations.

V. CONCLUSION

This paper proposes a novel mm-wave SDoF 6 × 2 D-MIMO architecture using off-the-shelf hardware based on a low-noise CU-inherited LO distribution concept. The architecture is demonstrated by the realization of a system with two distributed RRHs, each with three digitally controlled channels. Experimental results of a 6 × 2 distributed MU-MIMO at mm-wave with OFDM 64-QAM signals up to 748 MHz bandwidth are reported with EVM results satisfying 3GPP requirements. The results demonstrate the feasibility of the proposed hardware architecture for the realization of next-generation high-capacity wireless communication networks. Our demonstration can in the future be used for localizing/sensing studies.

ACKNOWLEDGMENT

The authors want to thank Xilinx for the donation of the Virtex UltraScale+ HBM VCU128 FPGA Evaluation Kit and the license to the Vivado software used for the FPGA development. The authors also want to thank Analog Devices for the donation of the EVAL-ADMV1013 Evaluation Board for this demonstration. The authors want to extend thanks to Keysight for the loan of the N9042B UXA X-Series Signal Analyzer during measurements.

REFERENCES

[1] Cisco, "Cisco Annual Internet Report," 2023. [Online]. Available: https://www.cisco.com/c/en/us/solutions/executive-perspectives/annual-internet-report/index.html
[2] Ericsson, "Ericsson Mobility Report," 2023. [Online]. Available: https://www.ericsson.com/en/reports-and-papers/mobility-report/mobility-visualizer
[3] W. Feng, Y. Wang *et al.*, "When mmWave Communications Meet Network Densification: A Scalable Interference Coordination Perspective," *IEEE Journal on Selected Areas in Communications*, vol. 35, no. 7, pp. 1459–1471, 2017.
[4] A. Shaikh and M. J. Kaur, "Comprehensive Survey of Massive MIMO for 5G Communications," in *2019 Advances in Science and Engineering Technology International Conferences (ASET)*, March 2019, pp. 1–5.
[5] E. Björnson and L. Sanguinetti, "Cell-Free versus Cellular Massive MIMO: What Processing is Needed for Cell-Free to Win?" in *2019 IEEE 20th International Workshop on Signal Processing Advances in Wireless Communications (SPAWC)*, July 2019, pp. 1–5.
[6] W. Roh and A. Paulraj, "Outage performance of the distributed antenna systems in a composite fading channel," in *Proceedings IEEE 56th Vehicular Technology Conference*, vol. 3, 2002, pp. 1520–1524.
[7] C. Fager, S. Rimborg *et al.*, "Comparison of Co-located and Distributed MIMO for Indoor Wireless Communication," in *2022 IEEE Radio and Wireless Symposium (RWS)*, 2022, pp. 83–85.
[8] E. Rådahl and S. Rimborg, "Simulations of the Capacity and Coverage for a Multi-User Distributed MIMO Network," Master's thesis, Chalmers University of Technology, 2009.
[9] C. Lim, Y. Tian *et al.*, "Evolution of Radio-Over-Fiber Technology," *J. Lightwave Technol.*, vol. 37, no. 6, pp. 1647–1656, Mar 2019.
[10] H. Al-Raweshidy and S. Komaki, "Radio over fiber technology for the next generation," *Radio over Fiber technologies for mobile communications networks*, 2002.
[11] A. H. M. R. Islam, M. Bakaul, and A. Nirmalathas, "Multilevel Modulations for Gigabit Access in a Simple Millimeter-Wave Radio-Over-Fiber Link," *IEEE Photonics Technology Letters*, vol. 24, no. 20, pp. 1860–1863, Oct 2012.
[12] D. Perez-Galacho, D. Sartiano, and S. Sales, "Analog Radio over Fiber Links for Future 5G Radio Access Networks," in *2019 21st International Conference on Transparent Optical Networks (ICTON)*, July 2019, pp. 1–4.
[13] D. Konstantinou, T. A. Bressner *et al.*, "5G RAN architecture based on analog radio-over-fiber fronthaul over UDWDM-PON and phased array fed reflector antennas," *Optics Communications*, vol. 454, p. 124464, 2020.
[14] L. Bogaert, J. Van Kerrebrouck *et al.*, "SiPhotonics/GaAs 28-GHz Transceiver With Reflective EAM for Laser-Less mmWave-Over-Fiber," *Journal of Lightwave Technology*, vol. 39, no. 3, pp. 779–786, Feb 2021.

[15] R. X. F. Budé, M. M. A. Versluis *et al.*, "Millimeter-Wave Outphasing using Analog-Radio over Fiber for 5G Physical Layer Infrastructure," in *2020 50th European Microwave Conference (EuMC)*, Jan 2021, pp. 288–291.
[16] J. Pérez Santacruz, E. Meyer *et al.*, "Outdoor mm-wave 5G/6G transmission with adaptive analog beamforming and IFoF fronthaul," *Scientific Reports*, vol. 13, no. 1, 2023.
[17] K. Ito, M. Suga *et al.*, "Passive beamformer based remote beamforming scheme for radio-over-fiber systems: Experimental demonstration using 28-GHz band reflectarray," *Optics Communications*, vol. 513, p. 128026, 2022.
[18] I. L. d. Paula, L. Bogaert *et al.*, "Air-Filled SIW Remote Antenna Unit with True Time Delay Optical Beamforming for mmWave-over-Fiber Systems," *Journal of Lightwave Technology*, pp. 1–15, 2022.
[19] A. Moerman, J. Van Kerrebrouck *et al.*, "Beyond 5G Without Obstacles: mmWave-over-Fiber Distributed Antenna Systems," *IEEE Communications Magazine*, vol. 60, no. 1, pp. 27–33, January 2022.
[20] R. Puerta, J. Yu *et al.*, "Single-Carrier Dual-Polarization 328-Gb/s Wireless Transmission in a D-Band Millimeter Wave 2 × 2 MU-MIMO Radio-Over-Fiber System," *Journal of Lightwave Technology*, vol. 36, no. 2, pp. 587–593, 2018.
[21] M. Sung, J. Kim *et al.*, "Demonstration of 5G Trial Service in 28 GHz Millimeter Wave using IFoF-Based Analog Distributed Antenna System," in *2019 Optical Fiber Communications Conference and Exhibition (OFC)*, March 2019, pp. 1–3.
[22] F. Olofsson, L. Aabel *et al.*, "Comparison of Transmitter Nonlinearity Impairments in externally modulated Sigma-Delta-over Fiber vs Analog Radio-over-Fiber links," in *2022 Optical Fiber Communications Conference and Exhibition (OFC)*. IEEE, 2022, pp. 1–3.
[23] N. Tawa, T. Kuwabara *et al.*, "28 GHz Over-the-Air Measurement using an OTFS Multi-User Distributed MIMO," in *2021 51st European Microwave Conference (EuMC)*, 2022, pp. 450–453.
[24] P. Zhu, Y. Yoshida *et al.*, "DSP-enhanced radio-over-fiber technologies for 5G-and-beyond wired-wireless convergence," *Journal of Optical Communications and Networking*, vol. 14, no. 8, pp. 595–605, 2022.
[25] J. Wang, Z. Jia *et al.*, "Delta-Sigma Modulation for Next Generation Fronthaul Interface," *Journal of Lightwave Technology*, vol. 37, no. 12, pp. 2838–2850, 2019.
[26] Y. Zhu, X. Fang *et al.*, "Radio-over-Fiber Transmission Supporting 65536-QAM at 25GHz Band with High-Pass Delta-Sigma Modulation and RF fading Mitigation," in *2022 Optical Fiber Communications Conference and Exhibition (OFC)*, 2022, pp. 1–3.
[27] L. Zhang, Z. Chen *et al.*, "Hybrid fiber-THz fronthaul supporting up to 16384-QAM-OFDM with the delta-sigma modulation," *Opt. Lett.*, vol. 47, no. 17, pp. 4307–4310, Sep 2022.
[28] F. Zhao, X. Yang *et al.*, "Demonstration of 4096QAM THz MIMO wireless delivery employing one-bit delta-sigma modulation," *Opt. Lett.*, vol. 47, no. 24, pp. 6361–6364, Dec 2022.
[29] J. Shi, J. Yu *et al.*, "4096-QAM OFDM THz-over-fiber MIMO transmission using delta-sigma modulation," *IEEE Photonics Technology Letters*, pp. 1–1, 2023.
[30] H. Li, M. Verplaetse *et al.*, "Real-Time 100-GS/s Sigma-Delta Modulator for All-Digital Radio-Over-Fiber Transmission," *Journal of Lightwave Technology*, vol. 38, no. 2, pp. 386–393, 2020.
[31] C.-Y. Wu, H. Li *et al.*, "Distributed Antenna System Using Sigma-Delta Intermediate-Frequency-Over-Fiber for Frequency Bands Above 24 GHz," *Journal of Lightwave Technology*, vol. 38, no. 10, pp. 2765–2773, May 2020.
[32] H. Bao, Z. S. He *et al.*, "Demonstration of Flexible mmWave Digital Beamforming Transmitter using Sigma-Delta Radio-Over-Fiber Link," in *2022 52th European Microwave Conference (EuMW)*, 2022.
[33] H. Bao, F. Ponzini, and C. Fager, "Wideband mm-wave Spectrum-Efficient Transmitter Using Low-Pass Sigma-Delta-over-Fiber Architecture," *IEEE Microwave and Wireless Technology Letters*, pp. 1–4, 2023.
[34] ——, "Flexible mm-Wave Sigma-Delta-Over-Fiber MIMO Link," *Journal of Lightwave Technology*, vol. 41, no. 14, pp. 4734–4742, July 2023.
[35] R. Schreier, "Delta Sigma Toolbox," Accessed: 2022-12-12. [Online]. Available: https://www.mathworks.com/matlabcentral/fileexchange/19-delta-sigma-toolbox
[36] I. C. Sezgin, M. Dahlgren *et al.*, "A Low-Complexity Distributed-MIMO Testbed Based on High-Speed Sigma–Delta-Over-Fiber," *IEEE Transactions on Microwave Theory and Techniques*, vol. 67, no. 7, pp. 2861–2872, July 2019.
[37] C.-Y. Wu, H. Li *et al.*, "Distributed Multi-User MIMO Transmission Using Real-Time Sigma-Delta-Over-Fiber for Next Generation Fronthaul Interface," *Journal of Lightwave Technology*, vol. 38, no. 4, pp. 705–713, Feb 2020.
[38] *5G; NR; Base Station (BS) radio transmission and reception (release 17) (V17.5.0)*, 3GPP, 2022, TS 38.104.
[39] M. Sung, J. Kim *et al.*, "RoF-Based Radio Access Network for 5G Mobile Communication Systems in 28 GHz Millimeter-Wave," *Journal of Lightwave Technology*, vol. 38, no. 2, pp. 409–420, 2020.
[40] A. Moerman, J. Van Kerrebrouck *et al.*, "mmWave-over-Fiber Distributed Antenna Systems for Reliable multi-Gbps Wireless Communication," in *2022 3rd URSI Atlantic and Asia Pacific Radio Science Meeting (AT-AP-RASC)*, May 2022, pp. 1–4.
[41] T. Nagayama, S. Akiba *et al.*, "Photonics-Based Millimeter-Wave Band Remote Beamforming of Array-Antenna Integrated With Photodiode Using Variable Optical Delay Line and Attenuator," *Journal of Lightwave Technology*, vol. 36, no. 19, pp. 4416–4422, 2018.

Husileng Bao (Student Member, IEEE) received the M.Sc. degree in electronics and communication engineering from the Beijing Institute of Technology, Beijing, China, in 2016. He worked as an engineer for Tsinghua University, Beijing, China until 2018. Then he joined Ericsson, Beijing, China. Since 2020, he has been working toward the Ph.D. degree as a Marie Curie early-stage-researcher with the Microwave Electronics Laboratory, Department of Microtechnology and Nanoscience (MC2), Chalmers University of Technology, Gothenburg, Sweden. His main research interests include MIMO communication and radio-over-fiber.

Filippo Ponzini Filippo Ponzini was born in Piacenza, Italy, in 1973. He received the master's degree in telecommunications engineering from the University of Parma, Italy. He was a Researcher in optical technologies with the Scuola Superiore Sant'Anna, Pisa, Italy. Since 2007, he has been with Ericsson Research. He is currently involved in optical datacenters architectures and optical networks and systems for 5G radio access networks. He has authored over 30 publications and international patents.

Christian Fager (Senior Member, IEEE) received the Ph.D. degree from the Chalmers University of Technology, Gothenburg, Sweden, in 2003. He is currently a Full Professor with the Chalmers University of Technology and Head of the Microwave Electronics Laboratory. He has authored or coauthored more than 200 publications in international journals and conferences. His current research interest includes energy efficient and linear transmitters for future wireless communication systems. He is an Associate Editor for IEEE Microwave Magazine and IEEE Microwave and Wireless Components Letters. He is a Representative for Sweden, Norway, and Iceland in the European Microwave Association (EuMA). He is a TPC Member of the IEEE MTT-S International Microwave Symposium and is also the Chair or Co-Chair of the 2020 or 2021 IEEE Topical Conference on RF/microwave Power Amplifiers, and TPC Co-Chair for the 2020 European Microwave Integrated Circuits Conference. He was the recipient of the Chalmers Supervisor of the Year Award in 2018 and the IEEE International Microwave Symposium Best Student Paper Award in 2002.